JACS
JOURNAL OF THE AMERICAN CHEMICAL SOCIETY

Article

pubs.acs.org/JACS

Heterogeneous Spin States in Ultrathin Nanosheets Induce Subtle Lattice Distortion To Trigger Efficient Hydrogen Evolution

Youwen Liu,[†] Xuemin Hua,[†] Chong Xiao,*[,†] Tengfei Zhou,[‡] Pengcheng Huang,[†] Zaiping Guo,[‡] Bicai Pan,[†] and Yi Xie*[,†]

[†]Hefei National Laboratory for Physical Sciences at the Microscale, Collaborative Innovation Center of Chemistry for Energy Materials, University of Science & Technology of China, Hefei, Anhui 230026, P. R. China

[‡]Institute for Superconducting and Electronic Materials, Australian Institute for Innovative Materials (AIIM), and School of Mechanical, Materials and Mechatronics Engineering, University of Wollongong, North Wollongong, NSW 2500, Australia

Supporting Information

ABSTRACT: The exploration of efficient nonprecious metal eletrocatalysis of the hydrogen evolution reaction (HER) is an extraordinary challenge for future applications in sustainable energy conversion. The family of first-row-transition-metal dichalcogenides has received a small amount of research, including the active site and dynamics, relative to their extraordinary potential. In response, we developed a strategy to achieve synergistically active sites and dynamic regulation in first-row-transition-metal dichalcogenides by the heterogeneous spin states incorporated in this work. Specifically, taking the metallic Mn-doped pyrite $CoSe_2$ as a self-adaptived, subtle atomic arrangement distortion to provide additional active edge sites for HER will occur in the $CoSe_2$ atomic layers with Mn incorporated into the primitive lattice, which is visually verified by HRTEM. Synergistically, the density functional theory simulation results reveal that the Mn incorporation lowers the kinetic energy barrier by promoting H−H bond formation on two adjacently adsorbed H atoms, benefiting H_2 gas evolution. As a result, the Mn-doped $CoSe_2$ ultrathin nanosheets possess useful HER properties with a low overpotential of 174 mV, an unexpectedly small Tafel slope of 36 mV/dec, and a larger exchange current density of 68.3 μA cm^{-2}. Moreover, the original concept of coordinated regulation presented in this work can broaden horizons and provide new dimensions in the design of newly highly efficient catalysts for hydrogen evolution.

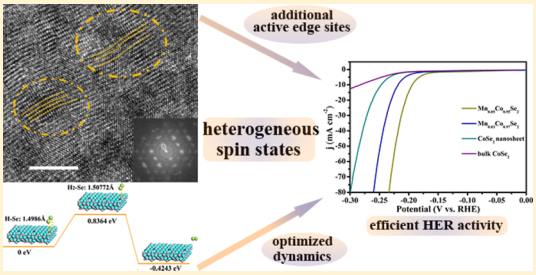

INTRODUCTION

Clean hydrogen evolution through electrochemistry underpins various innovative approaches to the pursuit of sustainable energy conversion technologies, which represent a serious scientific challenge driven by our increasing petroleum feedstock's consumption and bigger global population.[1−7] A critical element to overcome this challenge is the design of satisfactory electrocatalysts with low overpotential, a small Tafel slope, and a large exchange current to drive hydrogen evolution.[8] Illuminated by the burgeoning exploratory research, the economical and abundant metal dichalcogenides,[9−15] nitrides,[16−18] phosphides,[19−24] etc. have been proposed to replace the state-of-the-art Pt catalyst, the costliness and terrestrial scarcity of which impede practical utilization of hydrogen energy. Among the above new-type platinum-free catalysts, first-row-transition-metal dichalcogenides with an ideal atomic arrangement and low electrical resistance have been identified as potential catalysts of the hydrogen evolution reaction (HER), although a lack of fundamental active sites, limited by the thermodynamic driving force, tremendously impedes the intrinsic catalytic activity of the first-row-transition-metal dichalcogenides. In a recent development, through the DFT calculations of Dai's group,[13] the chalcogenide atoms at the edges of pyrite catalyst were found to be HER active sites analogous to MoS_2-type transition-metal dichalcogenides, providing a theoretical foundation to regulate the active sites on the atomic scale. In this regard, to maximize the number of exposed edge sites relative to bulk sites is a prerequisite for optimization of the catalytic activity of the first-row-transition-metal dichalcogenides in a similar fashion to MoS_2.[25,26] Focusing on this issue, several conventional strategies (such as amorphization[27,28] or ultrasmall nanoparticles[29,30]) were proposed; however, unfortunately, the obstacle of poor interparticle electron migration during the HER process was unavoidable. In this regard, the concept of introducing a subtle distortion of the atomic arrangement into the ultrathin nanosheets emerged in response to the above-mentioned contradiction,[31,32] which benefited from the maintenance of the original electron conjugated system along the two-dimensional plane and was conducive to quick electron transfer between the domain boundaries. Stimulated by the aforesaid concept, the construction of a subtle distortion on the atomic basal planes is a useful strategy for optimizing the HER active edge sites of first-row-transition-metal dichalcogenides on the basis of guaranteed robust electron transfer.

Received: January 25, 2016
Published: March 26, 2016

DOI: 10.1021/jacs.6b00858
J. Am. Chem. Soc. 2016, 138, 5087−5092

Under the circumstances, introducing heterogeneous spin states, namely, foreign metal atoms with similar atomic radius and electron configuration in the crystal lattice, could inevitably generate a local lopsided Coulomb force. The emergent micromechanically derived disturbance will consequently induce subtle distortion of the atomic arrangement, thus finally engineering additional exposed edge sites of first-row-transition-metal dichalcogenides for the HER. Synergistically, previous experimental and theoretical work has anticipated that the hydrogen adsorption kinetic energy barrier in the usual HER approach could be ameliorated by the incorporation of foreign metal atoms that can manipulate the electronic structure of the electrocatalyst.[13,33] More importantly, the distortion degree and electronic structure could be expediently and availably adjusted by the doping content. Inspired by the above insight, the incorporation of metal atoms has been considered to be a valid strategy to optimize synergistically the active sites and HER dynamics for adequately promoting HER activity in first-row-transition-metal dichalcogenides.

Among these pyrite dichalcogenides, $CoSe_2$, as a typical metallic material, possesses intrinsic high conductivity and ensures effective electron transfer during the electrocatalysis that is superior to electron transfer in other semiconductor pyrites.[12] Moreover, our group recently has achieved atomically thin $CoSe_2$ by a conventional liquid-phase exfoliation,[34] providing an existing platform to realize the above established model. Therefore, taking the metallic pyrite $CoSe_2$ as an example, conceptually subtle distortion of atomic arrangement, which is induced into the ultrathin nanosheets by the incorporation of heterogeneous Mn^{2+}, is first presented and rationally designed as a tactic to expose active edge sites for optimizing HER activity in this work. Furthermore, the Mn-doped $CoSe_2$ ultrathin nanosheets (MCSUNs) provide an opportunity to regulate the electronic structure to optimize the HER dynamics. As benefits of the synergistic modulation of additional active edge sites and the electrocatalytic kinetics, the subtle distortion of atomic arrangement confined on the MCSUNs yields a low overpotential of 174 mV, an unexpectedly small Tafel slope of 36 mV/dec, and a large exchange current density of 68.3 μA cm^{-2}, which, as comprehensive parameters, are comparable to those of the state-of-the-art non-noble-metal hydrogen evolution catalysts. Even more importantly, the original concept of coordinated regulation presented in this work can broaden our horizons in the design of new highly efficient catalysts for hydrogen evolution.

EXPERIMENTAL SECTION

Synthesis of Mn-Incorporated $CoSe_2$ Hybrid Precursors and MCSUNs. Lamellar hybrid Mn-incorporated $CoSe_2$/DETA (DETA stands for diethylenetriamine) products were prepared according to the literature.[34] The difference is that a certain molar ratio of $Co(CH_3COO)_2{\cdot}4H_2O$ and $Mn(CH_3COO)_2{\cdot}4H_2O$ (with total dose of 1 mmol) replaces the single $Co(CH_3COO)_2{\cdot}4H_2O$. In addition, the MCSUNs were obtained by the conventional liquid exfoliation method, as with the virgin $CoSe_2$ ultrathin nanosheets.[34]

Characterization. The atomistic structure information and microtopography were characterized by XRD on a Philips X'Pert Pro Super diffractometer with Cu Kα radiation (λ = 1.541 78 Å), field emission scanning electron microscopy (FE-SEM) on a JEOL JSM-6700F SEM, TEM on a H-7650 field emission electron microscope, HRTEM on a JEOL JEM-ARF200F, tapping-mode AFM on a DI Innova Multimode SPM platform, Raman spectroscopy on a Renishaw RM3000 micro-Raman system, and XPS spectrometry on a VG ESCALAB MKII X-ray photoelectron spectrometer with an Al Kα excitation source, respectively.

Electrode Preparation and Electrochemical Measurements. Electrochemical measurements were performed in a standard three-electrode electrochemical cell using an electrochemical workstation (CHI660B). A graphite rod, Ag/AgCl (PINE, 3 M KCl), and a glassy carbon electrode were used as counter, reference, and working electrodes, respectively. All cyclic voltammetry of the HER activity was conducted using 0.5 M H_2SO_4 electrolyte under continuous purging with 99.999% N_2 (Praxair) and at a sweep rate of 10 mV s^{-1}. Catalyst inks were typically made by dispersing 4 mg of catalyst in 1 mL of ethanol. After adding 30 μL of 0.05 wt % Nafion solution and ultrasonication for 30 min, an aliquot of 5 μL was pipetted onto the glassy carbon electrode to obtain the catalyst loading of 0.28 mg cm^{-2}. Finally, the as-prepared catalyst film was dried at room temperature. All the data were recorded after applying a number of potential sweeps until they were stable. Current density was normalized to the geometrical area of the working electrode. All the potentials in our paper are reported vs the reversible hydrogen electrode (RHE), based on the Nernst equation.

DFT Calculations. Our simulations were performed on the basis of a $CoSe_2$(210) slab model system. We have adopted slabs with three $CoSe_2$ layers consisting of 72 atoms ($Co_{24}Se_{48}$). The periodically repeated slabs were separated from their neighboring images by a 15-Å-wide vacuum in the direction perpendicular to the surface. We also substituted two Co atoms for two Mn atoms to investigate the effects of doping. All calculations in this work were performed using the VASP program, which employs the plane wave pseudopotential method to calculate the total energy within the framework of Kohn–Shan DFT. In our calculations, GGA+U with U = 1.0 eV is employed. The exchange and correlation interaction between electrons are treated by the Perdew–Burke–Ernzerhof (PBE) functional, and the projector-augmented wave (PAW) method with a plane–wave cutoff of 350 eV is adopted. A Monkhorst–Pack grid of size of 2 × 2 × 1 was used to sample the surface Brillouin zone. For the electronic self-consistency loop, a total energy convergence criterion of 1×10^{-4} eV is required. Lattice constants and internal coordinates of each system are fully optimized until residual Hellmann–Feynman forces are smaller than 0.01 eV/Å.

RESULTS AND DISCUSSION

Manganese-doped $CoSe_2$/DETA hybrid nanosheets [Figures S1 and S2, Supporting Information (SI)] with gradient Mn/Co mole ratios were fabricated by the solvothermal method using the recently reported binary solution.[35] Furthermore, the MCSUNs were obtained by our liquid exfoliation method. The molecular formulas for the MCSUNs were identified as $Mn_{0.05}Co_{0.95}Se_2$ and $Mn_{0.03}Co_{0.97}Se_2$ by the inductively coupled plasma (ICP) technique. Further intensive insights into the atomistic structure of the MCSUNs were acquired from the Raman spectra and X-ray diffraction (XRD) patterns, as shown in Figure 1a,b. The Raman peak of the $Mn_{0.05}Co_{0.95}Se_2$ ultrathin nanosheets corresponds well with that of bulk $CoSe_2$, and no other peaks, such as $MnSe_2$ or MnSe, can be detected, and suggesting the high purity in the MCSUNs. In addition, this conclusion was further confirmed by X-ray photoelectron spectroscopy (XPS), as shown in Figure S3 (SI). Meanwhile, to illuminate the exposed plane of MCSUNs, the XRD patterns of the $Mn_{0.05}Co_{0.95}Se_2$ film assembled layer-by-layer from the as-obtained ultrathin nanosheets clearly displays the sole (210) diffraction peak of bulk $CoSe_2$, which provides undoubtable evidence for the (210) exposed facet of $Mn_{0.05}Co_{0.95}Se_2$. The visible and incontestable evidence extracted by the elemental mapping images (Figure 1c–f) demonstrates the homogeneous spatial distributions of Mn, Co, and Se in the basal plane and the incorporation of Mn into the $CoSe_2$ crystal lattice. The transparent transmission electron microscope (TEM) image

DOI: 10.1021/jacs.6b00858
J. Am. Chem. Soc. 2016, 138, 5087–5092

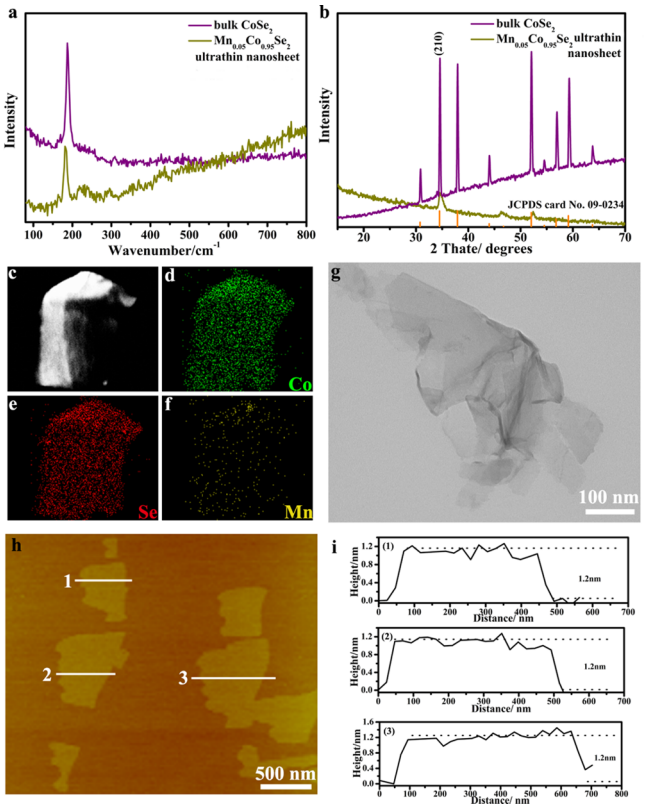

Figure 1. Atomistic structure information and microtopography of $Mn_{0.05}Co_{0.95}Se_2$ ultrathin nanosheets: (a) Raman spectra, (b) XRD pattern for an ultrathin nanosheet based film fabricated by layer-by-layer assembly, (c–f) Elemental mapping images, (g) TEM image, and (h, i) AFM image and corresponding height profiles. The profiles 1–3 correspond to the lines labeled as such in part h.

(Figure 1g) reveals that the $Mn_{0.05}Co_{0.95}Se_2$ product has an ultrathin nanosheet configuration. The specific thickness of the $Mn_{0.05}Co_{0.95}Se_2$ ultrathin nanosheets was evaluated by atomic force microscopy (AFM) [Figures 1h,i and S4 (SI)]. Notably, the uniform thickness was measured to be ~1.2 nm, which basically corresponds to the $CoSe_2$ ultrathin nanosheets in our previous report,[34] demonstrating the successful exfoliation of $Mn_{0.05}Co_{0.95}Se_2$. Consequently, the above characterization results unequivocally demonstrate that the $Mn_{0.05}Co_{0.95}Se_2$ was fabricated in the ultrathin nanosheet conformation with the nanosheets being 1.2 nm in thickness.

In the light of the latest research results of Dai's group, the chalcogen atoms on the edges of the first-row-transition-metal dichalcogenide catalysts were found to be HER active sites.[13] On this occasion, the design of an appropriate distortion of the atomic arrangement and grain boundaries in the atomically thin nanosheets could provide the opportunity to augment the number of marginal chalcogen atom active sites. The distortion of the atomic arrangement induced by the heterogeneous Mn spin states incorporated into the $CoSe_2$ ultrathin nanosheets has presented a suitable model for the use of controllable grain boundaries to boost HER performance. To verify the above expectation, the magnetic field dependence of magnetization ($M-H$) curves at 300 K of $CoSe_2$ ultrathin nanosheets and MCSUNs were used to investigate the heterogeneous spin states. As displayed in Figure 2a, the $M-H$ curves confirm the expected intense ferromagnetic nature of MCSUNs, where the curves exhibit an evident hysteresis loop. By clear contrast, very weak ferromagnetism in the virgin $CoSe_2$ ultrathin nanosheet is manifested by the fact that the $M-H$ hysteresis loop exhibits inconspicuous. Further, the coercivity of $Mn_{0.05}Co_{0.95}Se_2$, $Mn_{0.03}Co_{0.97}Se_2$ and virgin $CoSe_2$ ultrathin nanosheet are 350, 130, and 3.4 Oe, respectively. The significant differences of magnetic behavior between virgin $CoSe_2$ and the MCSUNs further confirm the success of introducing the heterogeneous spin states. Moreover, the confinement of the distorted atomic arrangement to the basal plane was visually confirmed by the HRTEM images and corresponding fast Fourier transform (FFT) patterns, as displayed in Figure 2b–d. The relatively regular atomic arrangement in the crystal lattice can be observed on the basal surfaces of the $CoSe_2$ ultrathin nanosheets. The identified lattice spacings of 0.238 and 0.14 nm can be assigned to the (211) and (420) facets, respectively, which indicate that the exposed lattice planes of the MCSUNs are the (210) facets, in agreement with the XRD results. Interestingly, the slight rotations that are marked in Figure 2d can be observed in some parts of the HRTEM image of MCSUNs, and they still maintain the original two-dimensional arrangement and electron conjugated system. When the Mn molar ratio increases to 0.05 in $Mn_{0.05}Co_{0.95}Se_2$, a more obvious disordered arrangement on the individual surface is obtained. Considering the successful introduction of the heterogeneous spin states, the formation of an innovative subtle atomic arrangement distortion may be related to the following two issues (Figure 2e–g): (i) the localized Coulomb interaction around the Mn atoms arising from the introduction of the incoordinate electron spin and (ii) the mismatch in the degree of Jahn–Teller distortion between the Mn–Se (for Mn^{2+}, $t_{2g}^5e_g^0$, t_{2g} orbitals are unevenly occupied, yielding a weak Jahn–Teller effect) and Co–Se (for Co^{2+}, $t_{2g}^6e_g^1$, e_g orbitals are unevenly occupied, yielding a strong Jahn–Teller effect) coordination octahedra.[36] In order to directly estimate the extent of disorder, the rotational angles determined by two end points of a diffraction arc and the central spot of the FFT have been introduced, as in the previous literature.[37,38] The virgin $CoSe_2$, $Mn_{0.03}Co_{0.97}Se_2$, and $Mn_{0.05}Co_{0.95}Se_2$ ultrathin nanosheets exhibit degrees of disorder of 4.6%, 11.6%, and 23.3%, respectively. It is our understanding that the distorted atomic arrangement induced by the extraneous spin states, namely, metal ions incorporated in the first-row-transition-metal dichalcogenide ultrathin nanosheets, represents a new ideal material model for optimizing HER active sites, and a schematic illustration of the regulated atomic arrangement is presented as Figure 2e–g.

In order to confirm the hypothesis, the electrocatalytic hydrogen evolution activities of the MCSUNs were investigated. The polarization curves for the MCSUNs, along with those of $CoSe_2$ ultrathin nanosheets, bulk $CoSe_2$, and commercial Pt/C (Figure S5, SI) for comparison, are presented in Figure 3a. All of the MCSUNs possess low overpotential to drive the electrode reaction, and among them, $Mn_{0.05}Co_{0.95}Se_2$ exhibits the exceptionally low value of 174 mV (determined from the semilog plot shown in Figure 3b), suggesting outstanding hydrogen evolution activity. In striking contrast, the $CoSe_2$ ultrathin nanosheets and bulk $CoSe_2$ exhibited inadequate HER activity, with the considerably large onset overpotentials of ~224 and 255 mV, respectively. Meanwhile, the drive current density of −10 mA cm^{-2}, which is a characteristic value related to solar fuel conversion, can be achieved at a exceptionally small overpotential of 195 mV for $Mn_{0.05}Co_{0.95}Se_2$ catalyst. The $Mn_{0.03}Co_{0.97}Se_2$ and $CoSe_2$

DOI: 10.1021/jacs.6b00858
J. Am. Chem. Soc. 2016, 138, 5087–5092

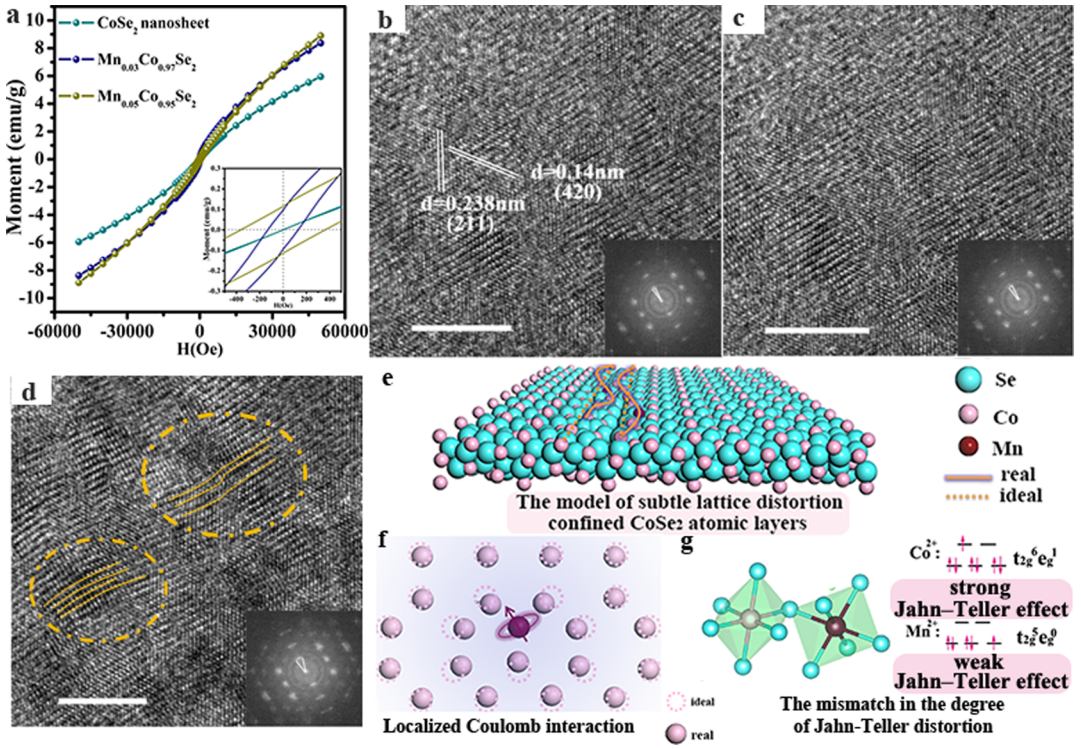

Figure 2. (a) The magnetic field dependence of magnetization (M–H) curve at 300 K. HRTEM images and corresponding FFT patterns (insets) for (b) virgin $CoSe_2$, (c) $Mn_{0.03}Co_{0.97}Se_2$, and (d) $Mn_{0.05}Co_{0.95}Se_2$, in which each (211) and (420) lattice spacing can be well-indexed. Scale bars: 5 nm. The subtle distortion regions are marked by the orange lines in part c. (e–g) Schematic representations of the formation mechanism for the subtle distortion of atomic arrangement through the incorporated heterogeneous spin states.

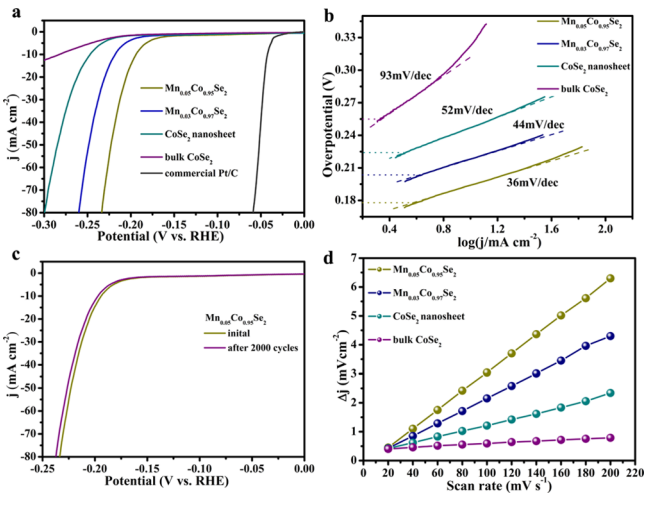

Figure 3. (a) Polarization curves. (b) Corresponding Tafel slopes. (c) Stability test. (d) The differences in current density variation ($\Delta J = J_a - J_c$) at an overpotential of 0.15 V plotted against scan rate fitted to a linear regression enable the estimation of C_{dl}.

ultrathin nanosheets require 218 and 247 mV overpotentials to achieve the reference current density of −10 mA cm^{-2}, respectively. Moreover, the extremely large current density, which is positively related to the amount of H_2 evolution on the $Mn_{0.05}Co_{0.95}Se_2$ ultrathin nanosheets, is 80 mA cm^{-2} with η = 233 mV, which is the 18 times larger than that of the $CoSe_2$ ultrathin nanosheets, illustrating the exceptionally enhanced HER activity in the MCSUNs. Further assessment of the HER activity was extracted from the Tafel slope, which is a significant parameter that reveals hydrogen evolution dynamics. As shown in Figure 3b, the unexpectedly low Tafel slope of ~36 mV/dec was obtained for the $Mn_{0.05}Co_{0.95}Se_2$ ultrathin nanosheets, a value that is obviously lower than the ~52 mV/dec for $CoSe_2$ ultrathin nanosheets and ~93 mV/dec for bulk $CoSe_2$. As far as we know, the Tafel slope is also favorable in comparison to all the reported noble-metal-free HER electrocatalysts, illustrating the robust HER kinetics of the $Mn_{0.05}Co_{0.95}Se_2$ ultrathin nanosheets. The exchange current density, j_0, which can be extracted from the Tafel slope by applying the extrapolation method (as listed in Table S1, SI), was employed to evaluate the inherent HER activity.[16] The j_0 of ~68.3 μA cm^{-2} for $Mn_{0.05}Co_{0.95}Se_2$ ultrathin nanosheets considerably outbalances the value of 10.3 μA cm^{-2} for the pure $CoSe_2$ ultrathin nanosheets, which is attributed to the unique distorted atomic arrangement that is confined in the plane and yields a significant excess of active sites. Apart from the HER activity, the durability is a pivotal dimension for a good electrocatalyst. To verify the long-term stability of the $Mn_{0.05}Co_{0.95}Se_2$ ultrathin nanosheets under strong-acid conditions, this electrocatalyst was cycled continuously for 2000 cycles. As displayed in Figure 3c, the insignificant decline in the overpotential and current density under cycling indicates that the $Mn_{0.05}Co_{0.95}Se_2$ ultrathin nanosheets have exceptional stability, which may give this catalyst real applications. Besides, the structure and morphology of ultrathin nanosheets catalyst exhibit negligible change after 2000 CV cycles (Figure S6, SI). Furthermore, the electrochemical double-layer capacitance (C_{dl}), which is expected to be linearly proportional to the effective surface area, was measured to evaluate the effective electrochemical surfaces of the various catalysts.[39,40] As shown in Figures 3d and S7 and Table S1 (SI), the $Mn_{0.05}Co_{0.95}Se_2$ ultrathin nanosheets exhibit the largest C_{dl} of ~16.25 μF, far above the

DOI: 10.1021/jacs.6b00858
J. Am. Chem. Soc. 2016, 138, 5087–5092

value of the pure $CoSe_2$ ultrathin nanosheets, indicating the high exposure of effective active sites, agreeing with the degree of disorder. On the basis of the systematic electrochemical measurements, the integrated superior catalytic parameters (including low overpotential, small Tafel slope, large exchange current, large double-layer capacitance, and large current density) undoubtedly confirm that the distorted atomic arrangement confined in the MCSUNs leads to exceptional HER activity, making it a competitive HER catalyst to replace Pt in real-world application.

Apart from the regulation of catalytic active sites, variation of the electronic structure will occur with the incorporation of foreign spin states in the crystal lattice, and as a consequence, the kinetic energy barrier of the HER will inevitably be modified. The Tafel slopes are widely regarded as a powerful method for determining the elementary and rate-determining step of the hydrogen evolution reaction. The Tafel slope of 36 mV/dec indicates that the Volmer–Tafel mechanism applies for the MCSUNs. (The detailed mechanism is displayed in Figure 4a.) Furthermore, the rate-determining step is the Tafel

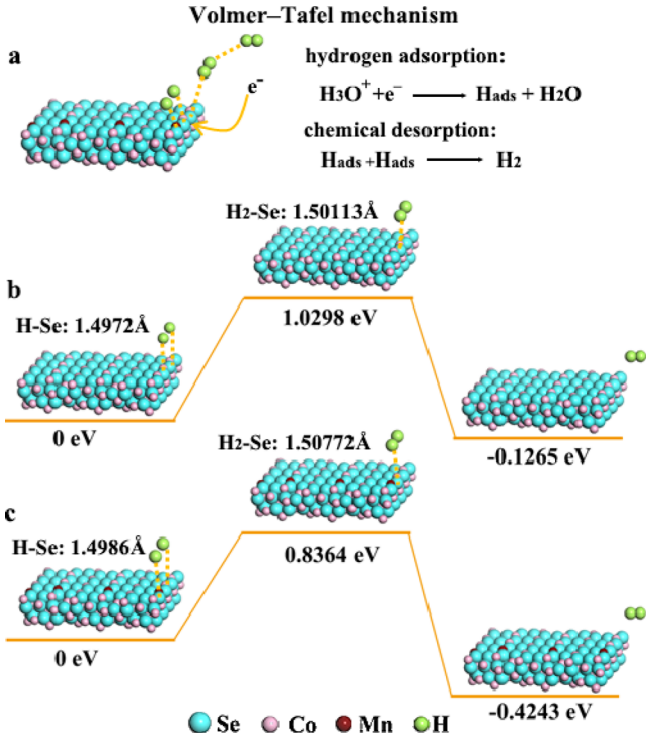

Figure 4. (a) Schematic representation of the HER pathway by the Volmer–Tafel mechanism. (b, c) The kinetic energy barrier profiles of the hydrogen evolution reaction on the edge sites of virgin $CoSe_2$ and MCSUNs.

reaction between two adjacent adsorbed H atoms, H_{ads} (H_{ads} + H_{ads} → H_2). Under the circumstances, the HER rate-determining process, including adsorption, activation, and the reaction energy-barrier of the electrocatalyst, was simulated by DFT modeling, which is a useful tool for elucidating the electrocatalysis reaction mechanism. As shown in Figure 4b, the bond length of H_{ads}–Se on the edge Se sites of MCSUNs was estimated to be 1.4986 Å, longer than the 1.4972 Å on the edge Se sites of $CoSe_2$ nanosheets, which indicates the relatively weak H_{ads}–Se bonds on the MCSUNs and is, in turn, conducive to the formation of H–H by the recombination of two adjacently adsorbed H_{ads}. Furthermore, the activation barrier of the H–H bond formation from adjacently adsorbed H_{ads} on the MCSUNs was simulated to be 0.8364 eV, obviously lower than that on $CoSe_2$ nanosheets of 1.0298 eV, agreeing with the bond length results. Similarly, the H_2 molecule adsorption on the MCSUNs surface possesses a simulated bond length of 1.50772 Å, larger than the 1.50113 Å for Se sites on $CoSe_2$ nanosheets, suggesting that Mn incorporation is more favorable for releasing H_2 gas during the HER. In conclusion, the Mn incorporation lowers the kinetic energy barrier by promoting H–H bond formation on two adjacently adsorbed H_{ads}, leading to H_2 gas evolution.

CONCLUSION

In conclusion, conceptually distorted atomic arrangement confined in MCSUNs is first presented and demonstrated to be a good model for the exposure of additional edge active sites on the atomic scale to optimize HER performance. In detail, the MCSUNs were first successfully fabricated by ordinary liquid exfoliation of homogeneous Mn-doped $CoSe_2$/DETA hybrid nanosheets, as verified by the Raman spectra, XRD patterns, elemental mapping, TEM, and AFM. Furthermore, the distorted atomic arrangements were directly visualized by HRTEM, confirming that more of the edge active sites were generated for HER catalysis. Synergistically, the Mn incorporation lowers the kinetic energy barrier by promoting H–H bond formation on two adjacently adsorbed H_{ads}, as predicted by the DFT simulation. With the benefits of simultaneous regulation of the active sites and dynamic pathways, the distortion of the atomic arrangement that is confined to the MCSUNs exhibits exceptional HER activity, manifesting a low overpotential of 174 mV, an unexpectedly small Tafel slope of 36 mV/dec, and a large exchange current density of 68.3 μA cm^{-2}, which outbalance the values for virgin $CoSe_2$ ultrathin nanosheets, as well as the most-reported platinum-free catalysts. The successful coordinated regulation of the active sites and optimization of the dynamical process for HER catalysts may broaden our horizons in the design of next-generation electrocatalysts.

ASSOCIATED CONTENT

Supporting Information

The Supporting Information is available free of charge on the ACS Publications website at DOI: 10.1021/jacs.6b00858.

Scheme for the formation of MCSUNs, characterization of Mn–$CoSe_2$/DETA hybrid precursors, XPS survey spectra for the MCSUNs, TEM and AFM of $Mn_{0.03}Co_{0.97}Se_2$ ultrathin nanosheets, structural characterization of $Mn_{0.05}Co_{0.95}Se_2$ ultrathin nanosheets after 2000 CV cycles, and comparison of HER parameters of various electrocatalysts (PDF)

AUTHOR INFORMATION

Corresponding Authors

*cxiao@ustc.edu.cn
*yxie@ustc.edu.cn

Notes

The authors declare no competing financial interest.

ACKNOWLEDGMENTS

This work was financially supported by National Basic Research Program of China (2015CB932302), National Natural Science

DOI: 10.1021/jacs.6b00858
J. Am. Chem. Soc. 2016, 138, 5087–5092

Foundation of China (21401182, 21331005, 11321503, 91422303, and U1532265), the Youth Innovation Promotion Association CAS (No. 2016392), the Key Laboratory of Neutron Physics (CAEP 2014DB02), and the Fundamental Research Funds for the Central University (WK2340000063 and WK 2060190027).

REFERENCES

(1) Greeley, J.; Jaramillo, T. F.; Bonde, J.; Chorkendorff, I. B.; Nørskov, J. K. *Nat. Mater.* **2006**, *5*, 909.
(2) Kibsgaard, J.; Chen, Z.; Reinecke, B. N.; Jaramillo, T. F. *Nat. Mater.* **2012**, *11*, 963.
(3) Turner, J. A. *Science* **2004**, *305*, 972.
(4) Voiry, D.; Yamaguchi, H.; Li, J.; Silva, R.; Alves, D. C. B.; Fujita, T.; Chen, M.; Asefa, T.; Shenoy, V. B.; Eda, G.; Chhowalla, M. *Nat. Mater.* **2013**, *12*, 850.
(5) Zheng, Y.; Jiao, Y.; Zhu, Y.; Li, L. H.; Han, Y.; Chen, Y.; Du, A.; Jaroniec, M.; Qiao, S. Z. *Nat. Commun.* **2014**, *5*, 3783.
(6) Wang, S. P.; Wang, J.; Zhu, M. L.; Bao, X. B.; Xiao, B. Y.; Su, D. F.; Li, H. R.; Wang, Y. *J. Am. Chem. Soc.* **2015**, *137*, 15753.
(7) Jin, H. Y.; Wang, J.; Su, D. F.; Wei, Z. Z.; Pang, Z. F.; Wang, Y. *J. Am. Chem. Soc.* **2015**, *137*, 2688.
(8) Subbaraman, R.; Tripkovic, D.; Strmcnik, D.; Chang, K. C.; Uchimura, M.; Paulikas, A. P.; Stamenkovic, V.; Markovic, N. M. *Science* **2011**, *334*, 1256.
(9) Gao, M. R.; Liang, J. X.; Zheng, Y. R.; Xu, Y. F.; Jiang, J.; Gao, Q.; Li, J.; Yu, S. H. *Nat. Commun.* **2015**, *6*, 5982.
(10) Xu, Y. F.; Gao, M. R.; Zheng, Y. R.; Jiang, J.; Yu, S. H. *Angew. Chem., Int. Ed.* **2013**, *52*, 8546.
(11) Kong, D.; Cha, J. J.; Wang, H.; Lee, H. R.; Cui, Y. *Energy Environ. Sci.* **2013**, *6*, 3553.
(12) Kong, D.; Wang, H.; Lu, Z.; Cui, Y. *J. Am. Chem. Soc.* **2014**, *136*, 4897.
(13) Wang, D. Y.; Gong, M.; Chou, H. L.; Pan, C. J.; Chen, H. A.; Wu, Y. P.; Lin, M. C.; Guan, M. Y.; Yang, J.; Chen, C. W.; Wang, Y. L.; Hwang, B. J.; Chen, C. C.; Dai, H. J. *J. Am. Chem. Soc.* **2015**, *137*, 1587.
(14) Peng, S.; Li, L.; Han, X.; Sun, W.; Srinivasan, M.; Mhaisalkar, S. G.; Cheng, F.; Yan, Q.; Chen, J.; Ramakrishna, S. *Angew. Chem., Int. Ed.* **2014**, *53*, 12594.
(15) Faber, M. S.; Dziedzic, R.; Lukowski, M. A.; Kaiser, N. S.; Ding, Q.; Jin, S. *J. Am. Chem. Soc.* **2014**, *136*, 10053.
(16) Cao, B.; Veith, G. M.; Neuefeind, J. C.; Adzic, R. R.; Khalifah, P. G. *J. Am. Chem. Soc.* **2013**, *135*, 19186.
(17) Chen, W. F.; Sasaki, K.; Ma, C.; Frenkel, A. I.; Marinkovic, N.; Muckerman, J. T.; Zhu, Y.; Adzic, R. R. *Angew. Chem., Int. Ed.* **2012**, *51*, 6131.
(18) Xie, J.; Li, S.; Zhang, X.; Zhang, J.; Wang, R.; Zhang, H.; Pan, B.; Xie, Y. *Chem. Sci.* **2014**, *5*, 4615.
(19) Jiang, P.; Liu, Q.; Liang, Y.; Tian, J.; Asiri, A. M.; Sun, X. *Angew. Chem., Int. Ed.* **2014**, *53*, 12855.
(20) Liu, Q.; Tian, J.; Cui, W.; Jiang, P.; Cheng, N.; Asiri, A. M.; Sun, X. *Angew. Chem.* **2014**, *126*, 6828.
(21) Tian, J.; Liu, Q.; Cheng, N.; Asiri, A. M.; Sun, X. *Angew. Chem., Int. Ed.* **2014**, *53*, 9577.
(22) Popczun, E. J.; Read, C. G.; Roske, C. W.; Lewis, N. S.; Schaak, R. E. *Angew. Chem., Int. Ed.* **2014**, *53*, 5427.
(23) Popczun, E. J.; McKone, J. R.; Read, C. G.; Biacchi, A. J.; Wiltrout, A. M.; Lewis, N. S.; Schaak, R. E. *J. Am. Chem. Soc.* **2013**, *135*, 9267.
(24) Xiao, P.; Sk, M. A.; Thia, L.; Ge, X.; Lim, R. J.; Wang, J. Y.; Lim, K. H.; Wang, X. *Energy Environ. Sci.* **2014**, *7*, 2624.
(25) Karunadasa, H. I.; Chang, C. J.; Long, J. R. *Nature* **2010**, *464*, 1329.
(26) Karunadasa, H. I.; Montalvo, E.; Sun, Y.; Majda, M.; Long, J. R.; Chang, C. J. *Science* **2012**, *335*, 698.
(27) Morales-Guio, C. G.; Hu, X. *Acc. Chem. Res.* **2014**, *47*, 2671.
(28) Merki, D.; Hu, X. *Energy Environ. Sci.* **2011**, *4*, 3878.
(29) Hinnemann, B.; Moses, P. G.; Bonde, J.; Jørgensen, K. P.; Nielsen, J. H.; Horch, S.; Chorkendorff, I.; Nørskov, J. K. *J. Am. Chem. Soc.* **2005**, *127*, 5308.
(30) Wang, T.; Liu, L.; Zhu, Z.; Papakonstantinou, P.; Hu, J.; Liu, H.; Li, M. *Energy Environ. Sci.* **2013**, *6*, 625.
(31) Xie, J.; Zhang, J.; Li, S.; Grote, F.; Zhang, X.; Zhang, H.; Wang, R.; Lei, Y.; Pan, B.; Xie, Y. *J. Am. Chem. Soc.* **2013**, *135*, 17881.
(32) Xie, J.; Zhang, H.; Li, S.; Wang, R.; Sun, X.; Zhou, M.; Zhou, J.; Lou, X.; Xie, Y. *Adv. Mater.* **2013**, *25*, 5807.
(33) Deng, J.; Li, H.; Xiao, J.; Tu, Y.; Deng, D.; Yang, H.; Tian, H.; Li, J.; Ren, P.; Bao, X. *Energy Environ. Sci.* **2015**, *8*, 1594.
(34) Liu, Y.; Cheng, H.; Lyu, M.; Fan, S.; Liu, Q.; Zhang, W.; Zhi, Y.; Wang, C.; Xiao, C.; Wei, S.; Ye, B.; Xie, Y. *J. Am. Chem. Soc.* **2014**, *136*, 15670.
(35) Gao, M. R.; Yao, W. T.; Yao, H. B.; Yu, S. H. *J. Am. Chem. Soc.* **2009**, *131*, 7486.
(36) Englman, R. *The Jahn−Teller Effect in Molecules and Crystals*; Wiley-Interscience: New York, 1972; p 139.
(37) Huang, P. Y.; Ruiz-Vargas, C. S.; van der Zande, A. M.; Whitney, W. S.; Levendorf, M. P.; Kevek, J. W.; Garg, S.; Alden, J. S.; Hustedt, C. J.; Zhu, Y.; Park, J.; McEuen, P. L.; Muller, D. A. *Nature* **2011**, *469*, 389.
(38) van der Zande, A. M.; Huang, P. Y.; Chenet, D. A.; Berkelbach, T. C.; You, Y.; Lee, G. H.; Heinz, T. F.; Reichman, D. R.; Muller, D. A.; Hone, J. C. *Nat. Mater.* **2013**, *12*, 554.
(39) Lukowski, M. A.; Daniel, A. S.; English, C. R.; Meng, F.; Forticaux, A.; Hamers, R. J.; Jin, S. *Energy Environ. Sci.* **2014**, *7*, 2608.
(40) Lukowski, M. A.; Daniel, A. S.; Meng, F.; Forticaux, A.; Li, L.; Jin, S. *J. Am. Chem. Soc.* **2013**, *135*, 10274.

DOI: 10.1021/jacs.6b00858
J. Am. Chem. Soc. 2016, 138, 5087−5092